Cell Reports, Volume *20*

Supplemental Information

Distortion of the Actin A-Triad Results in Contractile Disinhibition and Cardiomyopathy

Meera C. Viswanathan, William Schmidt, Michael J. Rynkiewicz, Karuna Agarwal, Jian Gao, Joseph Katz, William Lehman, and Anthony Cammarato

Supplemental Figures

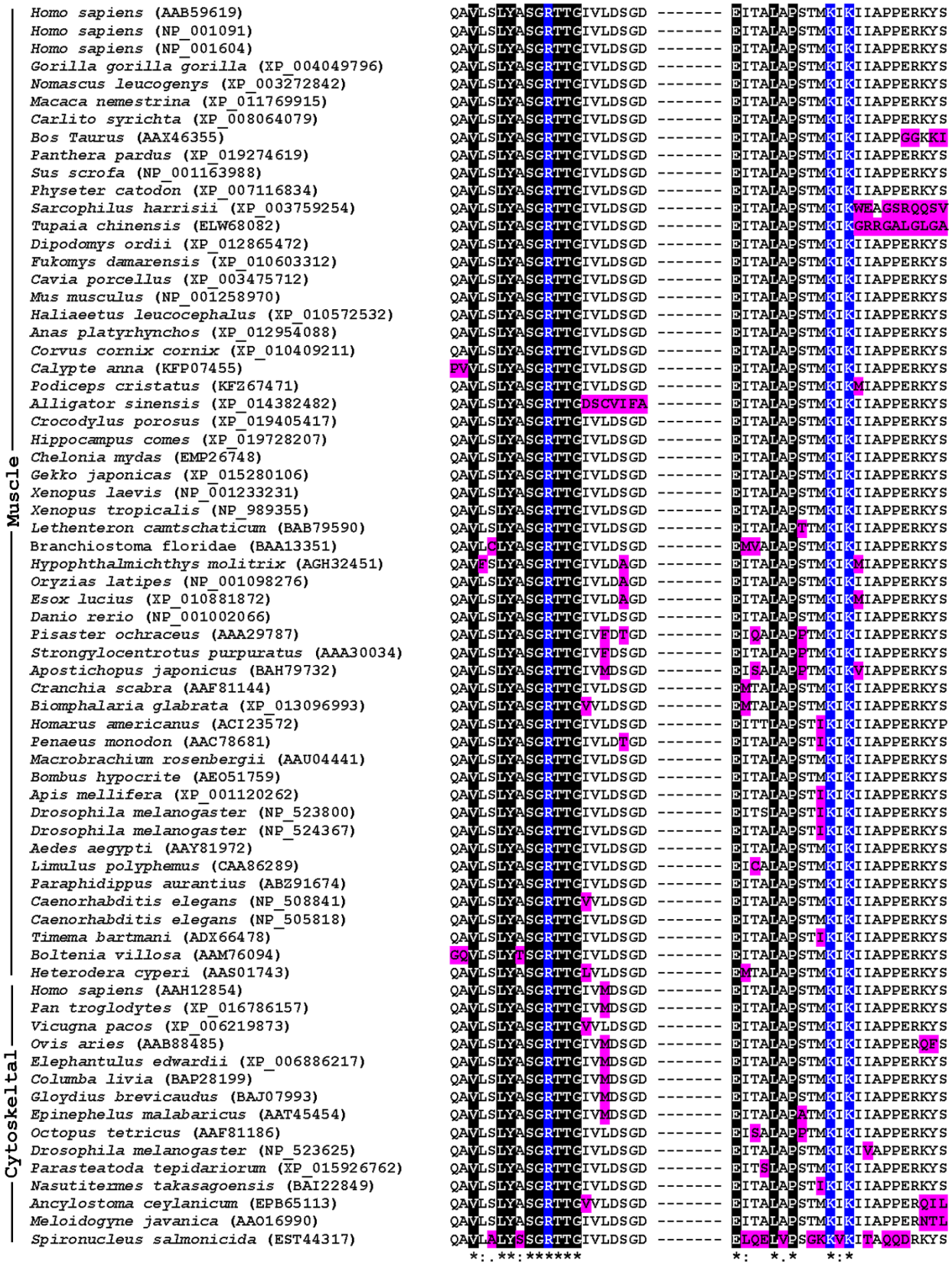

Figure S1 Related to Figure 1: Sequence alignment illustrates evolutionary conservation of actin A-triad residues. A BLASTp-based query of the 189 amino acid region that encompasses the human ACTC "A-triad" (from A144 through P332) identified 800 hits of muscle and cytoskeletal actins from various phyla throughout the animal kingdom. Among the 800, Clustal Omega multiple sequence alignment revealed ~30% identity of the 189 residue stretch. R147, K326, and K328 of the actin A-triad were among the amino acids exhibiting 100% conservation. 70 full-length muscle and cytoskeletal actin sequences were aligned (above) to demonstrate the extent of sequence variation in the A-triad vicintity. Amino acids immediately around the "A-triad" residues (blue) are displayed for reference. Identical residues are shaded black. Residues that differ from those of the human ACTC query sequence are highlighted pink. GenBank accession numbers are shown in parantheses.

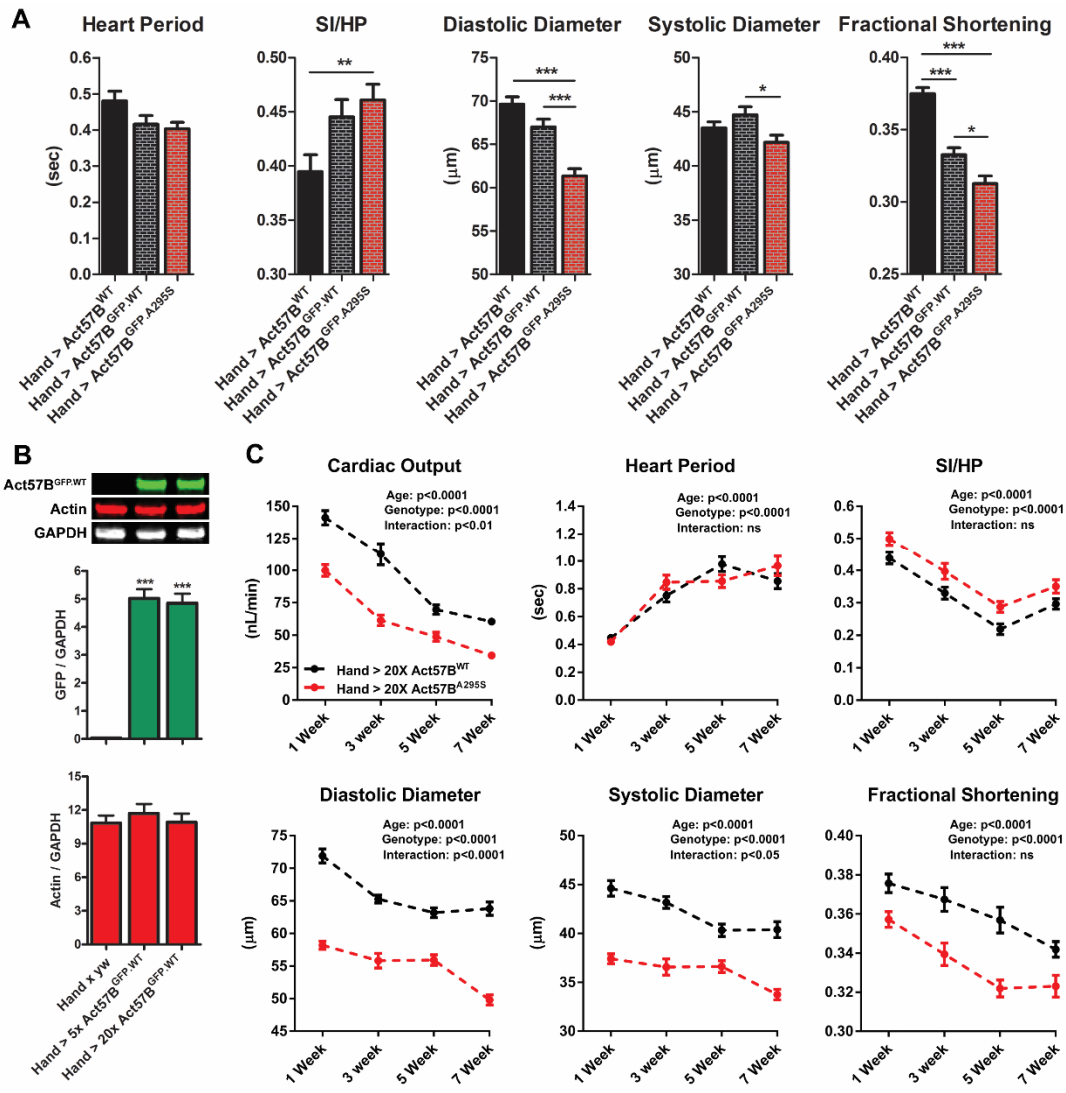

Figure S2 Related to Figure 3: Heart-specific expression of *GFP-actin* impacts cardiac performance, while expression of *20XUAS-Act57B^{A295S}* restricts cardiac dimensions and alters contractile properties akin to *5XUAS-Act57B^{A295S}*. (A) Semi-automated optical heartbeat analysis of three-week-old *Hand-Gal4 > 5XUAS-Act57B$^{GFP.WT}$* and *Hand-Gal4 > 5XUAS-Act57B$^{GFP.A295S}$* females revealed that the N-terminal GFP-tag on actin influences and masks A295S-mediated cardiac phenotypes. Data are presented as mean ± SEM (n = 37-45 for each genotype). Significance was assessed via one-way ANOVAs with Bonferroni multiple comparison tests. *$p \leq 0.05$; **$p \leq 0.01$; ***$p \leq 0.0001$ **(B)** In an attempt to increase expression of transgenic actin we generated additional fly lines that harbored *Act57B* transgenes preceded by 20 tandem Upstream Activating Sequences. These lines included *20XUAS-Act57B$^{GFP.WT}$*, *20XUAS-Act57B^{WT}*, and *20XUAS-Act57B^{A295S}*. Quantitative western blot analysis was employed to assess the levels of Act57B$^{GFP.WT}$, endogenous cardiac actin, and GAPDH from the hearts of *Hand-Gal4 x yw*, *Hand-Gal4 > 5XUAS-Act57B$^{GFP.WT}$*, and *Hand-Gal4 > 20XUAS-Act57B$^{GFP.WT}$*. No differences in abundance of Act57B$^{GFP.WT}$ or endogenous cardiac actin relative to GAPDH were detected in the hearts of *5XUAS* vs. *20XUAS* lines. As expected, both *Hand-Gal4 > 5XUAS-Act57B$^{GFP.WT}$* and *Hand-Gal4 > 20XUAS-Act57B$^{GFP.WT}$* hearts contained significantly higher Act57B$^{GFP.WT}$ relative to *Hand-Gal4 x yw*. GFP and actin intensities were measured and normalized to that of GAPDH from six biological replicates (40 hearts per biological replicate) with three technical replicates each. Data are presented as mean ± SEM. Significance was assessed via one-way ANOVAs with Bonferroni multiple comparison tests. ***$p \leq 0.0001$ **(C)** Semi-automated optical heartbeat analysis of *Hand-Gal4 > 20XUAS-Act57B^{WT}* vs. *Hand-Gal4 > 20XUAS-Act57B^{A295S}* resolved reductions in cardiac

dimensions, fractional shortening, and cardiac output coupled with prolonged systolic periods (elevated Systolic Interval / Heart Period) in mutant hearts over time. Two-way ANOVAs revealed significant genotype- and age-related alterations in cardiac physiological parameters. Data are presented as mean ± SEM (n = 35 – 36). The variant-associated effects were nearly identical to those observed with the *5XUAS* constructs (Figure 3C). See also Table S2.

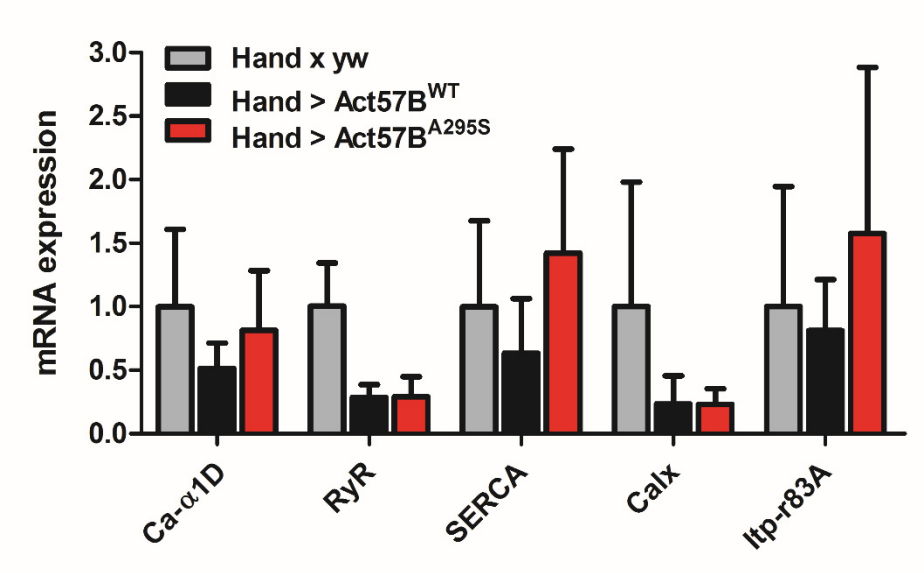

Figure S3 Related to Figure 4: A295S actin expression does not alter expression of Ca^{2+} handling genes in the heart. Quantitative polymerase chain reaction measurements of L-type Ca^{2+} channel, ryanodine receptor, sarcoplasmic reticulum Ca^{2+}-ATPase, Na/Ca exchanger, and inositol-3-phosphate receptor transcript levels, normalized to GAPDH transcript levels, in hearts of *Hand-Gal4 > UAS-Act57B^{WT}* and *Hand-Gal4 > UAS-Act57B^{A295S}* relative to *Hand-Gal4* x *yw* control. Values represent the average (± SEM) of four biological replicates (15 hearts per biological replicate) with three technical replicates each. One-way ANOVAs with Bonferroni post hoc tests revealed no significant differences in the expression of Ca^{2+}-handling genes between *Hand-Gal4* x *yw*, *Hand-Gal4 > UAS-Act57B^{WT}*, and *Hand-Gal4 > UAS-Act57B^{A295S}* hearts.

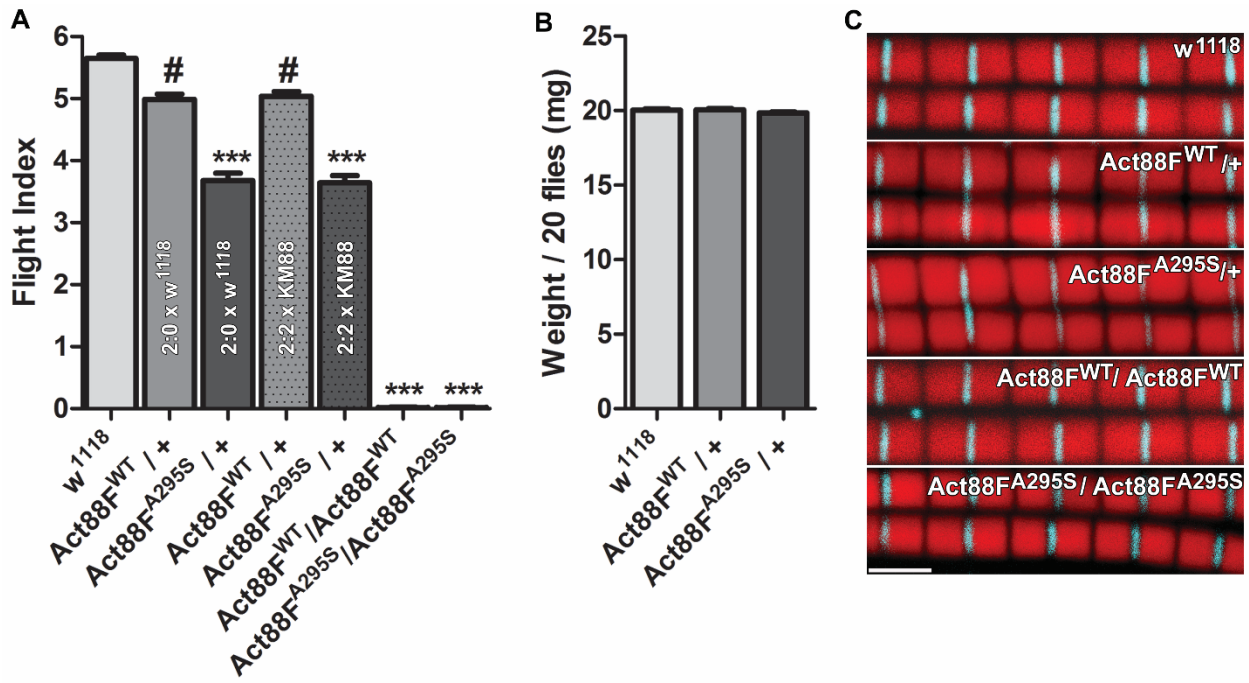

Figure S4 Related to Figures 5 and 6: A295S actin impairs *Drosophila* flight ability without altering thin filament lengths. (A) Flies heterozygous for the *Act88F^{WT}* transgene (*Act88F^{WT}*/+) had a small but significant reduction in flight ability relative to *w^{1118}* as ascertained by customary flight assays (Drummond et al., 1991). In contrast, *Act88F^{A295S}*/+ heterozygotes had substantially reduced flight compared to both *Act88F^{WT}*/+ heterozygotes and *w^{1118}* controls. Two independent lines, generated by different mating schemes, verified the altered flight ability of the WT- and A295S- actin expressing heterozygotes. 2:0 x *w^{1118}* refers to the scheme that resulted in heterozygotes whereby flies homozygous for the transgene in an endogenous IFM-actin null background were backcrossed to *w^{1118}*; 2:2 x KM88 refers to the scheme whereby flies with two copies of transgenic actin and 2 copies of endogenous actin were crossed with an IFM-null actin line (*KM88*) to generate heterozygotes. Importantly, *Act88F^{WT}*/*Act88F^{WT}* and *Act88F^{A295S}*/*Act88F^{A295S}* homozygotes completely lacked flight ability. Data are presented as mean ± SEM (n = 226 – 258). Significance was assessed via one-way ANOVA with the Kruskal-Wallis test. $^{\#}p \leq 0.05$; $^{***}p \leq 0.0001$ **(B)** Weights of 10 sets of 20 flies each were measured for *w^{1118}*, *Act88F^{WT}*/+, and *Act88F^{A295S}*/+ and averaged. Data are presented as mean ± SEM. One-way ANOVA with Bonferroni's multiple comparison test revealed no significant differences in fly weights. **(C)** Representative confocal images of IFM myofibrils from *w^{1118}*, *Act88F^{WT}*/+, *Act88F^{A295S}*/+, *Act88F^{WT}*/*Act88F^{WT}*, and *Act88F^{A295S}*/*Act88F^{A295S}* used for thin filament length measurements and for single sarcomere image averaging in Figure 6B, 6C. Myofibrils were labeled with Alexa568-phalloidin (red) and Cy5- mouse anti-α-actinin (cyan). Scale bar = 2.5 µm.

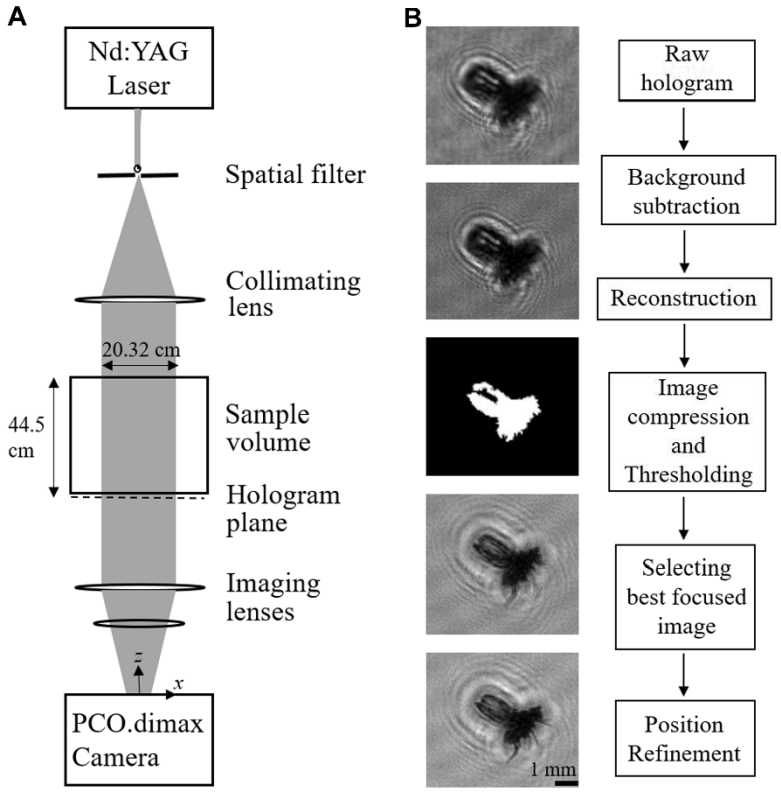

Figure S5 Related to Figure 5 and Experimental Procedures: Depiction of the digital 3D holography imaging technique. Three-dimensional holography is a volumetric imaging technique involving two stages: recording of the hologram and reconstruction of the original 3D field. Acquisition consists of illuminating an object with coherent light and recording the interference between light scattered from the object and a known reference wave. The simplest optical setup, inline holography, is the least demanding in terms of spatial resolution, and is well-suited for reconstruction of 3D distributions of multiple small objects. In this case, the same beam is used for illuminating the sample and as a reference wave. Part of the light is scattered by the object(s) and interferes with the remaining undisturbed component. Digital holography involves acquisition of holograms on digital media at varying magnifications, followed by numerical reconstruction. Background information and a comprehensive list of references is provided in Sheng et al (Sheng et al., 2006). Digital holography has helped characterize droplet dynamics in clouds (Fugal et al., 2004), marine organism motion (Malkiel et al., 2003), shearing of oil droplets (Gopalan and Katz, 2010), shapes of cells (Carl et al., 2004), and the behavior of fruit flies (Kumar et al., 2016).

Here, the technique was used to track the flight trajectories and behavior of various fruit fly genotypes in a relatively large sample volume. **(A)** Illustration of the optical setup of the inline digital holography system. The laser beam was filtered and collimated to illuminate the plexiglass fly chamber (i.e. sampling volume). Two imaging lenses placed beyond the sample volume facilitated transmission of the hologram to the CMOS camera. Holograms were recorded at 400 fps, at a 0.1905X magnification with 2016 x 2016 resolution. **(B)** Illustration of the steps involved in reconstruction of the 3D field. Each raw hologram was processed for background subtraction using holograms acquired from imaging an empty sample volume. Threshold adjustments were implemented to detect each fly in a compressed image field, and focus refinement performed to identify a clearly resolved position of the fly.

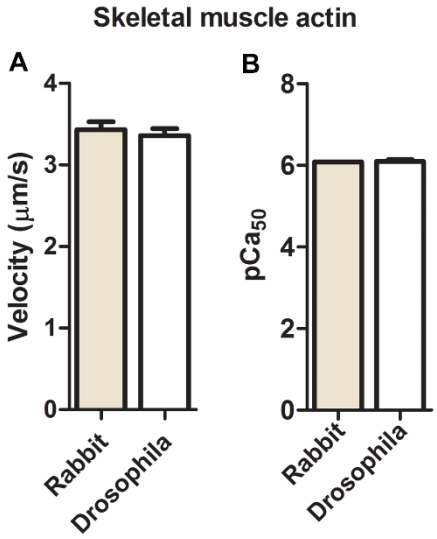

Figure S6 Related to Figure 7: *Drosophila* Act88F and rabbit skeletal muscle F-actin have identical unregulated sliding velocities and regulated pCa_{50} values. (A) F-actin derived from IFMs of w^{1118} *Drosophila* moved at the same average velocity as rabbit skeletal muscle F-actin with a high proportion of motile filaments. Velocities of 25 filaments from each animal were measured and compared using an unpaired *t*-test. Data are presented as mean ± SEM. **(B)** The Ca^{2+} concentration that yields half maximal activation (pCa_{50}) of thin filaments reconstituted using *Drosophila* or rabbit skeletal muscle actin in conjunction with vertebrate cardiac Tn-Tm, was identical. Velocities of 20-25 filaments were measured at each Ca^{2+} concentration, and mean velocities were plotted as a function of Ca^{2+} and fit to the Hill equation to determine the pCa_{50} for both groups. Significance was assessed using an unpaired *t*-test, and data shown are pCa_{50} ± SEM derived from the fits.

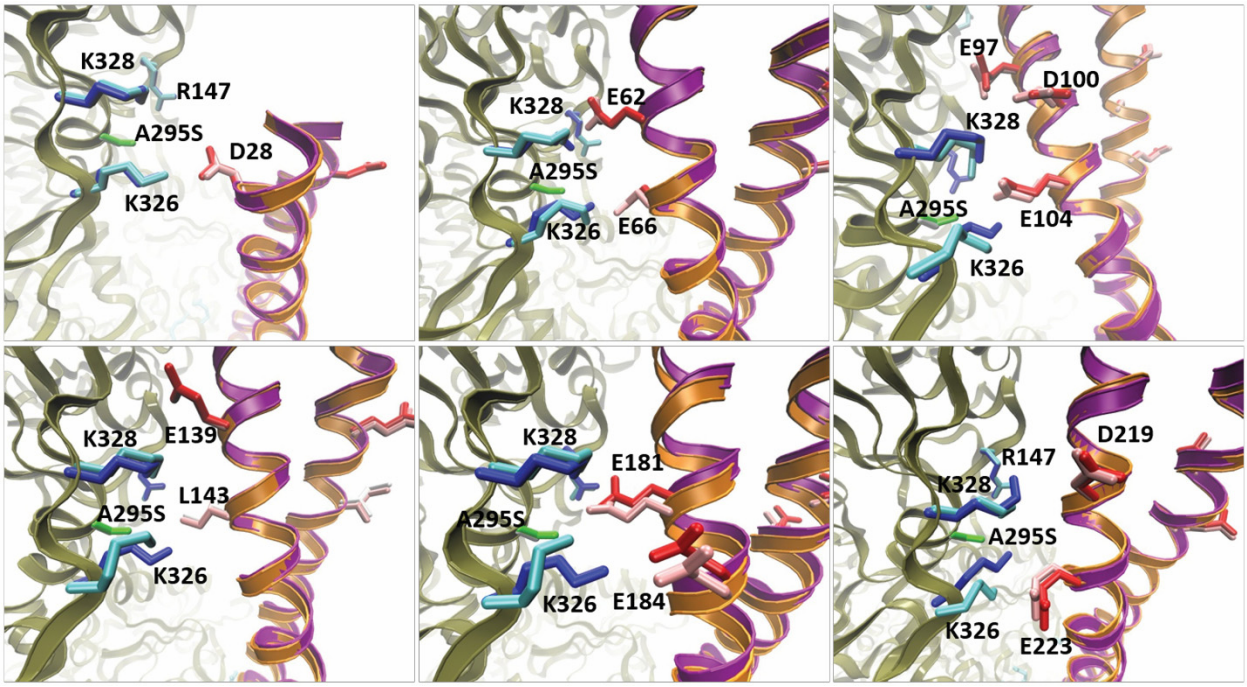

Figure S7 Related to Figure 7: Interactions of the A-triad with tropomyosin acidic residues at the minimum point in the energy landscapes. Actin (tan) and Tm (orange for wildtype and purple for A295S mutant) are rendered as ribbons. The side chains of the A-triad are shown in light blue (wildtype) and blue (mutant), with the mutant Ser side chain in green. The interacting side chains of Tm are colored pink (wildtype) and red (mutant). Note the summation of such small mutation-derived deviations in side chain orientations, which account for the distorted electrostatic interaction energy landscape, could bias Tm away from the A/B- and closer to the C-state configuration. See also Tables S3 and S4.

Table S1 Related to Figure 3: Effects of the A295S actin mutation (behind 5XUAS repeats) on the *Drosophila* heart. Two-way ANOVA results can be found in Figure 3C.

	Heart Period (Mean ± SEM)	**SI/HP** (Mean ± SEM)	**Diastolic Diameter** (Mean ± SEM)	**Systolic Diameter** (Mean ± SEM)	**Fractional Shortening** (Mean ± SEM)	**Cardiac Output** (Mean ± SEM)
Hand x yw **1wk (n=37)**	0.37 ± 0.02	0.42 ± 0.02	68.05 ± 1.15	43.80 ± 0.95	0.38 ± 0.01	122.74 ± 4.37
Hand > Act57B ^{WT} **1wk (n=35)**	0.38 ± 0.02	0.45 ± 0.02	68.53 ± 1.04	42.57 ± 0.84	0.38 ± 0.01	129.42 ± 3.65
Hand > Act57B ^{A295S} **1wk (n=38)**	0.36 ± 0.01	0.52 ± 0.01	63.74 ± 0.91	42.12 ± 0.71	0.34 ± 0.01	89.67 ± 5.63
Hand x yw **3wk (n=46)**	0.56 ± 0.03	0.40 ± 0.02	61.61 ± 0.58	43.00 ± 0.56	0.35 ± 0.01	110.12 ± 4.09
Hand > Act57B ^{WT} **3wk (n=45)**	0.46 ± 0.02	0.39 ± 0.02	69.61 ± 0.85	43.50 ± 0.58	0.37 ± 0.01	116.83 ± 4.90
Hand > Act57B ^{A295S} **3wk (n=45)**	0.50 ± 0.02	0.47 ± 0.02	62.97 ± 0.71	42.28 ± 0.63	0.32 ± 0.01	83.08 ± 4.58
Hand x yw **5wk (n=35)**	0.75 ± 0.05	0.34 ± 0.02	64.80 ± 0.98	41.78 ± 0.75	0.36 ± 0.01	84.55 ± 3.83
Hand > Act57B ^{WT} **5wk (n=36)**	0.87 ± 0.06	0.31 ± 0.02	68.23 ± 0.71	42.54 ± 0.63	0.36 ± 0.01	84.19 ± 4.07
Hand > Act57B ^{A295S} **5wk (n=34)**	0.74 ± 0.05	0.39 ± 0.02	57.59 ± 1.45	38.14 ± 0.90	0.32 ± 0.01	52.21 ± 3.60
Hand x yw **7wk (n=35)**	0.89 ± 0.05	0.32 ± 0.02	66.81 ± 0.84	40.33 ± 0.44	0.37 ± 0.01	65.37 ± 3.36
Hand > Act57B ^{WT} **7wk (n=36)**	0.79 ± 0.04	0.33 ± 0.02	64.70 ± 0.66	41.85 ± 0.60	0.35 ± 0.01	67.62 ± 2.23
Hand > Act57B ^{A295S} **7wk (n=35)**	0.86 ± 0.04	0.39 ± 0.02	56.74 ± 0.90	36.87 ± 0.47	0.31 ± 0.01	29.84 ± 1.36

Table S2 Related to Figure 3: Effects of the A295S actin mutation (behind 20XUAS repeats) on the *Drosophila* heart. Two-way ANOVA results can be found above, in Figure S2.

	Heart Period (Mean ± SEM)	**SI/HP** (Mean ± SEM)	**Diastolic Diameter** (Mean ± SEM)	**Systolic Diameter** (Mean ± SEM)	**Fractional Shortening** (Mean ± SEM)	**Cardiac Output** (Mean ± SEM)
Hand > 20xAct57B ^{WT} **1wk (n=36)**	0.45 ± 0.02	0.44 ± 0.02	71.90 ± 1.09	44.61 ± 0.80	0.41 ± 0.01	141.24 ± 5.59
Hand > 20xAct57B ^{A295S} **1wk (n=35)**	0.42 ± 0.02	0.50 ± 0.02	58.18 ± 0.62	37.41 ± 0.50	0.36 ± 0.01	99.89 ± 4.47
Hand > 20xAct57B ^{WT} **3wk (n=35)**	0.75 ± 0.05	0.33 ± 0.02	65.27 ± 0.60	43.16 ± 0.61	0.34 ± 0.01	112.67 ± 8.45
Hand > 20xAct57B ^{A295S} **3wk (n=35)**	0.85 ± 0.05	0.40 ± 0.02	55.83 ± 1.13	36.57 ± 0.83	0.32 ± 0.01	61.49 ± 4.06
Hand > 20xAct57B ^{WT} **5wk (n=35)**	0.98 ± 0.05	0.22 ± 0.02	63.18 ± 0.74	40.33 ± 0.64	0.36 ± 0.01	69.65 ± 3.69
Hand > 20xAct57B ^{A295S} **5wk (n=35)**	0.85 ± 0.05	0.28 ± 0.02	55.92 ± 0.80	36.61 ± 0.60	0.32 ± 0.01	48.67 ± 3.59
Hand > 20xAct57B ^{WT} **7wk (n=36)**	0.86 ± 0.05	0.30 ± 0.02	63.81 ± 1.04	40.40 ± 0.81	0.37 ± 0.01	60.44 ± 1.77
Hand > 20xAct57B ^{A295S} **7wk (n=35)**	0.97 ± 0.07	0.35 ± 0.02	49.80 ± 0.77	33.75 ± 0.54	0.32 ± 0.01	34.44 ± 1.97

Table S3 Related to Figure 7: **Distances between selected actin and tropomyosin residues from the minimized structures, derived from the electrostatic interaction landscapes, for wildtype and A295S F-actin-tropomyosins.** See also Figure S7.

Actin residue	Tm residue	A295S (Å)	WT (Å)	A295S - WT (Å)
Lys326	Asp28	5.56	5.24	0.32
Lys326	Glu62	7.12	7.31	-0.19
Lys326	Glu66	4.22	3.89	0.33
Lys326	Glu104	3.33	4	-0.67
Lys326	Glu181	4.26	3.75	0.51
Lys326	Glu184	4.29	5.82	-1.53
Lys326	Glu223	5.38	5.37	0.01
				$\bar{x}$ = -0.17
Lys328	Glu62	3.28	3.36	-0.08
Lys328	Glu97	6.97	7.66	-0.69
Lys328	Asp100	6.68	7.65	-0.97
Lys328	Glu104	2.69	3.13	-0.44
Lys328	Glu139	6.1	6.09	0.01
Lys328	Glu181	2.86	2.77	0.09
Lys328	Asp219	5.68	7.68	-2
				$\bar{x}$ = -0.59

Table S4 Related to Figure 7. Electrostatic interaction energies (kcal/mol) calculated between tropomyosin and the indicated residues of wildtype or A295S actin. See also Figure S7.

	R147	K326	K328	A-Triad	Overall
A295S	-250.90	-816.40	-949.85	-2017.15	-2220.96
WT	-264.59	-828.33	-877.59	-1970.50	-2164.62
(A295S – WT)	13.69	11.92	-72.26	-46.65	-56.34

Supplemental Experimental Procedures

Multiple sequence alignment to evaluate actin "A-triad" conservation
To evaluate conservation of the actin "A-triad" a 189-residue query sequence, spanning A144 through P332 of *Homo sapiens* cardiac actin (ACTC), was searched against the NCBI "non-redundant protein sequences database (nr)" for the most similar protein sequences, via the blastp algorithm. 1000 hits were identified. These were filtered to exclude non-actin proteins. 800 were finally categorized that included muscle and cytoskeletal actins from mammals, birds, reptiles, amphibians, fishes, echinoderms, mollusks, arthropods, flies, and worms. 70 full-length actin sequences were selected, which represented isoforms from the various orders, and aligned using the Clustal Omega multiple sequence alignment program to identify conservation of the "A-triad" and to demonstrate homology.

Construction of *20XUAS-Act57B* transgenes
In addition to *5XUAS* transgenes, we also generated *UAS-Act57B* constructs behind 20 tandem UAS repeats in an attempt to increase transgenic actin expression. The pJFRC7 vector with 20XUAS repeats was kindly shared by Dr. Adam Cohen (Harvard University, Cambridge, MA, USA). $Act57B^{GFP.WT}$, $Act57B^{WT}$, and $Act57B^{A295S}$ cDNA, from the pUASTattB constructs, were inserted into the pJFRC7 vector behind the UAS repeats using the NotI and XbaI restriction sites.

All vectors included the *Drosophila miniwhite* (w^+) gene for selection of successful genomic transformation based on pigmented eye color.

Generation of transgenic *Drosophila*
All constructs were injected into *attp40 Drosophila* embryos for PhiC31 integrase-mediated site-specific transgenesis (transgene cytolocation 25C7) by Genetic Services, Inc. Surviving adults from the pUASTattB and pJFRC7 transgene injections were crossed with *yw Drosophila*. Transformed progeny were screened for pigmented eye color and backcrossed into the *yw* background to generate stable transgenic lines. Non-transformed flies, also crossed into the *yw* background, served as controls for all studies involving *UAS-Act57B* lines.

Surviving adults from the pattB injections were crossed with w^{1118} *Drosophila*. Transformed progeny were selected and backcrossed into the w^{1118} background to generate stable transgenic lines. Non-transformed flies were crossed into the w^{1118} background and used as controls for *Act88F*-based experiments.

For all lines, genomic DNA was isolated from whole flies using the DNeasy blood and tissue kit (Qiagen Inc.), and sequenced to verify integration of transgenic DNA.

Protein quantification
Quantitative western blot analysis was performed using hearts from *Hand-Gal4 x yw*, *Hand-Gal4 > 5XUAS-*$Act57B^{GFP.WT}$, and *Hand-Gal4 > 20XUAS-*$Act57B^{GFP.WT}$ *Drosophila* to determine if 20X UAS repeats drive increased expression relative to 5X. Hearts from 40 flies were pooled as one biological replicate, homogenized in Laemmli sample buffer, electrophoresed, and blotted onto a nitrocellulose membrane. Membranes were incubated with primary rabbit anti-actin (Proteintech), rabbit anti-GFP (R&D), and goat anti-GAPDH (Genscript) antibodies overnight at 4°C and then probed with Donkey anti-rabbit and Donkey anti-goat IRDye secondary antibodies (LI-COR Biosciences) for 60-90 min at room temperature. The membranes were subsequently scanned using an Odyssey Infrared Imager (λ = 700 and 800nm) and analyzed using Odyssey Application Software (v3.030, LI-COR Biosciences). Mean values (±SEM) of actin and GFP intensities, normalized to respective GAPDH intensities, were determined. Quantification was performed on six independent biological replicates with three technical replicates each. Significance was assessed via one-way ANOVAs with Bonferroni's multiple comparison tests and reported at $p < 0.05$.

Cardiac physiological analysis
One-, three-, five-, and seven-week-old, female *Hand-Gal4 x yw*, *Hand-Gal4 > UAS-*$Act57B^{WT}$, and *Hand-Gal4 > UAS-*$Act57B^{A295S}$ and three-week-old *Hand-Gal4 > UAS-*$Act57B^{GFP.WT}$ and *Hand-Gal4 > UAS-*$Act57B^{GFP.A295S}$ semi-intact *Drosophila* hearts (n = 35-46) were prepared under oxygenated artificial hemolymph (AH) at 25°C as described by Vogler and Ocorr (Vogler and Ocorr, 2009). High-speed videos (120-150 fps) of beating hearts were recorded with a Hamamatsu Orca-Flash 2.8 digital camera on a Leica DM5000B DIC microscope fitted with a 10X

(0.30 N.A.) immersion lens. Cardiac performance was analyzed using Semi-automated Optical Heartbeat Analysis (SOHA), a free, custom-written motion analysis program (Fink et al., 2009), (Cammarato et al., 2015). M-modes, which provide an edge trace documenting heart wall movement over time, were generated via the program. Myogenic "cardiac output" of the *Drosophila* heart tube was calculated as described in Blice-Baum et al (Blice-Baum et al., 2017). Individual frames of beating hearts during peak diastole and peak systole, from the various ages and genotypes, were obtained from the high-speed videos. A two-dimensional cardiac area was determined for a defined length (l) of every heart for each cardiac cycle phase. The 2D area extended from abdominal segment two through four of the fly heart and was thus essentially rectangular. The average diameter of the heart during systole and diastole over the area was determined. This section of the heart tube was subsequently geometrically modeled as a cylinder. Hence, $\pi \cdot r^2 \cdot l$ was used to calculate volumes during peak diastole and systole and to ascertain "stroke volume" (diastolic volume – systolic volume). Cardiac output (nL/min) was determined as the product of stroke volume and heart rate. Significant differences in physiological parameters, between genotype and age, and interaction effects, were determined using two-way ANOVAs with Bonferroni's post-hoc tests. When measured values were not normally distributed, data were transformed logarithmically and significance assessed as above. Significance was reported at $p < 0.05$.

Quantitative polymerase chain reaction

Total RNA was isolated from dissected hearts of three-week-old *Hand-Gal4 x yw*, *Hand-Gal4 > UAS-Act57B^{WT}*, and *Hand-Gal4 > UAS-Act57B^{A295S}* female flies using the Quick-RNA microprep kit (Zymo Research Corp.). Reverse transcription polymerase chain reaction was performed using Qiagen QuantiTect Reverse Transcription Kits (Qiagen Inc.) and 10ng of RNA per reaction. Quantitative polymerase chain reaction was performed on a Bio-Rad CFX96 Real-Time PCR Detection System. Taqman primers targeting universally-transcribed regions of the L-type Ca^{2+} channel (*Ca-α1D*; Dm01807733), ryanodine receptor (*RyR*; Dm01842311), sarcoplasmic reticulum Ca^{2+}-ATPase (*SERCA*; Dm01820194), Na/Ca exchanger (*Calx*; Dm02136145), inositol-3-phosphate receptor (*Itp-r83A*; Dm02147941) and GAPDH (*Gapdh1*; Dm01843827) were used (ThermoFisher Scientific). Four independent experiments were performed, per gene, in triplicate using pools of 15 hearts per reaction. Significance was assessed using one-way ANOVAs followed by Bonferroni's multiple comparison tests and reported at $p < 0.05$.

Flight tests

Flight tests were performed on male and female *w^{1118}*, *Act88F^{WT}*/+, *Act88F^{A295S}*/+, *Act88F^{WT}*/*Act88F^{WT}*, and *Act88F^{A295S}*/*Act88F^{A295S} Drosophila* as described by Drummond et al. (Drummond et al., 1991). Newly eclosed flies were aged for 2 days at 25°C. Flies were released into the center of a plexiglass chamber with a light source positioned at the top and assigned a flight index based on direction of flight (6 for upward flight, 4 for horizontal, 2 for downward, or 0 for no flight). The average flight index of 226-258 flies was calculated for each genotype. Significance was assessed via the Kruskal-Wallis one-way ANOVA with Dunn's post hoc test and reported at $p < 0.05$.

Holography

Holography has been used in a variety of applications including velocity measurements that resolve flow in the inner part of turbulent boundary layers, diffusion of oil droplets in high-Reynolds number turbulence, and predator-prey interactions among swimming microorganisms (Katz and Sheng, 2010). Here, cinematic digital inline holography was implemented to track flight trajectories of two-day-old *w^{1118}* non-transgenic actin control, *Act88F^{WT}*/+, and *Act88F^{A295S}*/+ male and female *Drosophila*. The optical setup (Figure S5A) consisted of a diode-pumped, Nd:YAG solid state green laser (CrystaLaser QL532-500) operating at 400 Hz, which generated a 0.1 μJ/pulse laser beam. The beam was spatially filtered, expanded, and collimated to generate a 20.32 cm diameter wave-front that illuminated an 11.6×11.6×44.5 cm^3 sample volume. Imaging lenses placed on the opposing side of the sample volume transmitted the hologram plane. This plane coincided with the window of the facility to a high-speed CMOS camera (PCO.dimax) at a magnification of 0.1905X. The holograms were recorded at 400 fps at a resolution of 2016 X 2016 pixels. Each experiment involved data acquisition for 7.82 s, which provided a sequence of 3128 holograms. The magnification and spatial coordinates were calibrated by recording holograms of known dot arrays.

30 flies of a given genotype were released from a tube placed at the bottom of a 44.5×44.5×44.5 cm^3 transparent acrylic enclosure. A halogen lamp was anchored above the chamber to entice upward flight. The temperature was maintained at 24°C. A chart outlining the process of reconstructing holograms and detecting the flight trajectories of individual flies is illustrated in Figure S5B. Background subtraction, to remove non-uniformities in illumination, stationary objects, and variations in camera sensitivity, was initially performed. Several holograms of the sample

volume, recorded without flies, were averaged to obtain a characteristic mean intensity distribution. Holograms of upward flying *Drosophila* were then reconstructed numerically in a series of x-y planes along the depth direction over the entire sample volume. Reconstruction of flight trajectories involved a convolution of the intensity distribution in the hologram with the Rayleigh-Sommerfeld diffraction kernel as reported in Katz and Sheng (Katz and Sheng, 2010). Initially, reconstruction was performed every 7 mm, and then refined to 500 μm in volumes of interest where the flies were located, based on preliminary evaluation.

The detection process first identified where to search for flies in the x-y plane. This procedure was performed by: (i) Generation of a compressed image of the entire volume by maintaining the lowest intensity over z for each pixel. The resultant map was threshold adjusted and a 2D segmentation process identified the boundaries of each object. (ii) Generation of a corresponding compressed image containing the maximum intensity gradients over depth for each pixel. Then, following the hybrid method described in Gao et al (Gao et al., 2013), the two maps were multiplied, which provided a 2D map of the projection of all the objects in the sample volume. The z coordinates were then identified based on the plane with the maximum intensity gradient.

To re-create the trajectories of each fly, we took advantage of the relative sparsity of the fly population, which allowed us to follow the trajectory by selecting the nearest neighbors in successive frames. Subsequent manual evaluation resolved issues caused by rare crossing trajectories. Examining all the presumed in-focus images, the algorithm identified the one with the sharpest boundaries, which was selected as an "anchor". Then, the displacement between exposures was calculated, starting from this anchor. Results were compared to the maximum allowed speed of 2 m/s based on preliminary evaluation of the data and consistent with prior publications (Vogel, 1966). In cases where the displacement exceeded the allowed range, additional planes within the proper range were reconstructed every 500 μm and the edge detection procedure was repeated to identify an improved in-focus location. The final position uncertainty in the x and y directions was ~ 50 μm, corresponding to 1 pixel, and 1.7 mm in the z direction.

w^{1118} (n = 80), $Act88F^{WT}$/+ (n = 90), and $Act88F^{A295S}$/+ (n = 30) trajectories were evaluated to calculate a series of associated kinematic properties. Fitting polynomial curves to the trajectory of each fly, the following equations

$$\vec{v} = (\dot{x}, \dot{y}, \dot{z}) \qquad \vec{a} = (\ddot{x}, \ddot{y}, \ddot{z})$$

$$k = \frac{|\dot{r}\times\ddot{r}|}{|\dot{r}|^3} \qquad \tau = \frac{(\dot{r}\times\ddot{r})\cdot\dddot{r}}{|\dot{r}\times\ddot{r}|^2} \qquad R = \frac{1}{\sqrt{k^2+\tau^2}} \qquad |\omega| = \frac{|v|}{R} \qquad \vec{a}_{centripetal} = \frac{|v|^2}{R}\frac{\dot{r}\times(\ddot{r}\times\dot{r})}{|\dot{r}\times(\ddot{r}\times\dot{r})|}$$

were used for calculating the total velocity ($\vec{v}$) and acceleration ($\vec{a}$) vectors, the angular velocity magnitude ($|\omega|$), and the centripetal acceleration component, the latter signifying the ability of the fly to maneuver. Here, $r = (x, y, z)$ is the three-dimensional position of the fly, over-dots indicate time derivatives, R is the 3D radius of curvature, k is the in-plane curvature, and τ is out-of-plane curvature (i.e. torsion). Significance was assessed using nonparametric Kruskal-Wallis one-way ANOVAs followed by Dunn's multiple comparison tests and reported at $p < 0.05$.

Measurements of fly weight

For body weight measures, w^{1118}, $Act88F^{WT}$/+, and $Act88F^{A295S}$/+ *Drosophila* were sedated using FlyNap and separated into 10 cohorts of 20 flies each. Weights of the cohorts were averaged and compared using one-way ANOVA with Bonferroni's multiple comparison test. Significance was assessed at $p < 0.05$.

Indirect flight muscle imaging

Fluorescent microscopy was performed as described previously (Viswanathan et al., 2015) to examine gross IFM morphology of two-day-old male and female w^{1118}, $Act88F^{WT}$/+, $Act88F^{A295S}$/+, $Act88F^{WT}/Act88F^{WT}$, and $Act88F^{A295S}/Act88F^{A295S}$ *Drosophila*. Briefly, flies were anesthetized, heads and abdomens removed, and thoraces paraformaldehyde fixed. The thoraces were rinsed and arranged on a glass slide, snap frozen in liquid nitrogen, and bisected down the midsagittal plane using a razor blade. The samples were stained with Alexa568-phalloidin, rinsed, and imaged with an EVOS® FL Cell Imaging System (Life Technologies) at 4X magnification.

Sarcomere imaging
IFM myofibril imaging was carried out as previously described (Haigh et al., 2010),(Cammarato et al., 2011). Briefly, thoraces of two-day-old w^{1118}, $Act88F^{WT}/+$, $Act88F^{A295S}/+$, $Act88F^{WT}/Act88F^{WT}$, and $Act88F^{A295S}/Act88F^{A295S}$ flies were bisected after removing the heads and abdomens and paraformaldehyde fixed. The thoraces were rinsed, stained with Alexa568-phalloidin, and rinsed again. IFM fibers were carefully removed, myofibrils gently teased apart, and mounted and imaged on a Leica TCS SPE RGBV confocal microscope at 100X magnification. Measurement of thin filament lengths (n = 222-254) was performed using ImageJ (http://rsb.info.nih.gov/ij/). Significance was assessed via the Kruskal-Wallis one-way ANOVA with Dunn's post-hoc test.

Actin purification
Rabbit skeletal actin was purified via established procedures (Spudich and Watt, 1971),(Pardee and Spudich, 1982) from rabbit skeletal muscle acetone powder (Pelfreeze Biologicals Cat. #41995-1). Purified G-actin was polymerized to F-actin in buffer containing 4 mM imidazole, 100 mM KCl, 2 mM MgCl2, 1 mM NaN3, 0.5 mM ATP, and 1 mM DTT and stored on ice at 4°C. Absorbance at 280 nm, corrected for scattering at 320 nm, was used to determine F-actin concentration.

Wildtype non-transgenic IFM actin from w^{1118}, and transgenic IFM actin from $Act88F^{WT}/Act88F^{WT}$ and $Act88F^{A295S}/Act88F^{A295S}$ *Drosophila* were purified according to Razzaq, et al (Razzaq et al., 1999). Briefly, heads and abdomens were removed from ~40 flies and IFMs pulled and stored in a solution of York Modified Glycerol overnight at -20°C. Following a series of high and low salt extractions and low-speed spindowns, isolated actin was polymerized in high salt (to remove tropomyosin) and pelleted at 100,000 rpm in a Beckman TL-100 ultracentrifuge rotor. F-actin was subsequently conjugated with Alexa488-phalloidin in a 1:1 molar ratio and left overnight at 4°C to equilibrate. 10nM Alexa488-phalloidin-labelled F-actin was used for *in vitro* motility experiments.

***In vitro* motility**
Rabbit skeletal muscle, $Act88F^{WT}$, and $Act88F^{A295S}$ F-actin motility was measured via a standard *in vitro* motility assay using full-length, rabbit skeletal myosin at 100 µg/mL (Kron and Spudich, 1986), and Ca^{2+}-sensitivity of reconstituted thin filaments was determined via established procedural modifications (Liang et al., 2003). Myosin was introduced into a flow cell and allowed two minutes to bind a nitrocellulose-coated cover slip. The surface was blocked with 2 mg/ml BSA, myosin "dead heads" were non-reversibly bound to unlabeled actin filaments, and enzymatically active myosin was bound to ~10 nM Alexa488-phalloidin-labeled rabbit skeletal, *Drosophila* $Act88F^{WT}$, or $Act88F^{A295S}$ F-actin. For F-actin motility measures, a motility buffer (25 mM KCl, 4 mM $MgCl_2$, 1 mM EGTA, 25 mM imidazole pH 7.2, 10 mM DTT, 1 mM ATP, 2 mM dextrose, 17 units/ml glucose oxidase, 125 units/ml catalase, and 0.5% methyl cellulose) was then added and displacement of actin filaments was visualized and measured as described below. To assess the effects of Ca^{2+} on reconstituted thin filament activation, myosin-bound, phalloidin-labelled F-actin was first incubated with 300 nM bovine cardiac Tm and Tn in solution containing 25 mM KCl, 25 mM imidazole pH 7.2, 1 mM EGTA, and 4 mM $MgCl_2$. Following a 5 minute incubation period to fully saturate F-actin with Tm and Tn, Ca^{2+}-dependent motility of reconstituted thin filaments at 30°C was assessed using motility buffer containing 150 nM Tm and Tn, and varying amounts of Ca^{2+} (10^{-9} to 10^{-4} M). Imaging was performed on an Olympus IX73 microscope, and Alexa488-phalloidin was excited using an X-CITE 120 LED lamp and a 482/35 filter. Emitted light was captured at 536/40 and detected on a Hamamatsu Flash 4LT EMCCD camera at 1-4 fps. Videos were recorded using HCI imaging software, converted to multipage TIF's, and imported into ImageJ. Average velocities were determined via manual tracking (Meijering et al., 2012) of ~20-25 filaments at each Ca^{2+} concentration tested. This represented a single experiment. Of note, flow cells were partitioned into two separate chambers using double-stick tape to allow for parallel assessment of $Act88F^{WT}$ and $Act88F^{A295S}$ reconstituted thin filament Velocity:pCa relationships. This strategy minimizes flow cell-to-flow cell variability and more accurately reflects potential differences between filament types.

Three separate preparations of $Act88F^{WT}$ and $Act88F^{A295S}$ actin were performed. For F-actin motility, a single experiment was carried out on each individual preparation (n = 3). Weighted average velocities and standard errors from ~60-75 filaments were calculated as outlined below. Duplicate assessments were made on reconstituted thin filaments prepared from each biological replicate (n = 6). Therefore, there were ~120-150 thin filaments analyzed per genotype at each Ca^{2+} concentration. A weighted Ca^{2+}-sensitivity curve was generated by calculating weighted average velocities ($V_{Avg.weight}$) at each Ca^{2+} concentration as shown below:

$$V_{Avg,\,weight} = \frac{\sum_{n=1}^{6}\left[V_{Avg,\,n} \times x_n\right]}{\sum_{n=1}^{6} x_n}$$

where V_{Avg} is average filament velocity measured in n experiment, and x_n is the number of filaments analyzed. $V_{Avg.weight}$ values were plotted as a function of Ca^{2+} along with weighted standard errors ($S.E._{weight}$) determined from the weighted standard deviations, $S.D._{weight}$:

$$S.D._{weight} = \sqrt{\frac{\sum_{n=1}^{6}\left[\left(V_{Avg,\,n} - V_{Avg.weight}\right)^2 \times \left(x_n / \sum_{n=1}^{6} x_n\right)\right]}{\frac{n-1}{n}\sum_{n=1}^{6}\left[x_n \Big/ \sum_{n=1}^{6} x_n\right]}}$$

The weighted mean values for $Act88F^{WT}$ and $Act88F^{A295S}$ thin filaments were fit by the least squares method (GraphPad Prism) to a 3-parameter Hill equation of the form:

$$V_{avg} = \frac{V_{\max} \times x^h}{{K_d}^h + x^h}$$

where V_{avg} is the predicted velocity at a given Ca^{2+} concentration x, and the fit parameters are V_{max}, velocity at maximum Ca^{2+} activation, K_d, concentration of Ca^{2+} required to achieve 0.5* V_{max}, and h, the Hill coefficient.

Unpaired *t*-tests were used to evaluate significant differences in motility parameters between rabbit and *Drosophila* skeletal muscle F-actin and regulated thin filaments, while differences in $Act88F^{WT}$ and $Act88F^{A295S}$ F-actin were similarly assessed on the pooled and weighted data. For Ca^{2+} regulated motility experiments, pooled Velocity:Ca^{2+} data at each distinct [Ca^{2+}] were re-plotted, fit to the Hill equation, and significant differences in fit parameters (V_{max}, pCa_{50}, and cooperativity) determined via extra sum of squares F-tests, with $p < 0.05$ deemed significant.

Supplemental References:

Blice-Baum, A.C., Zambon, A.C., Kaushik, G., Viswanathan, M.C., Engler, A.J., Bodmer, R., and Cammarato, A. (2017). Modest overexpression of FOXO maintains cardiac proteostasis and ameliorates age-associated functional decline. Aging Cell *16*, 93-103.

Cammarato, A., Li, X.E., Reedy, M.C., Lee, C.F., Lehman, W., and Bernstein, S.I. (2011). Structural basis for myopathic defects engendered by alterations in the myosin rod. J Mol Biol *414*, 477-484.

Cammarato, A., Ocorr, S., and Ocorr, K. (2015). Enhanced assessment of contractile dynamics in *Drosophila* hearts. Biotechniques *58*, 77-80.

Carl, D., Kemper, B., Wernicke, G., and von Bally, G. (2004). Parameter-optimized digital holographic microscope for high-resolution living-cell analysis. Appl Optics *43*, 6536-6544.

Drummond, D.R., Hennessey, E.S., and Sparrow, J.C. (1991). Characterisation of missense mutations in the *Act88F* gene of *Drosophila melanogaster*. Mol Gen Genet *226*, 70-80.

Fink, M., Callol-Massot, C., Chu, A., Ruiz-Lozano, P., Izpisua Belmonte, J.C., Giles, W., Bodmer, R., and Ocorr, K. (2009). A new method for detection and quantification of heartbeat parameters in *Drosophila*, zebrafish, and embryonic mouse hearts. Biotechniques *46*, 101-113.

Fugal, J.P., Shaw, R.A., Saw, E.W., and Sergeyev, A.V. (2004). Airborne digital holographic system for cloud particle measurements. Appl Optics *43*, 5987-5995.

Gao, J., Guildenbecher, D.R., Reu, P.L., and Chen, J. (2013). Uncertainty characterization of particle depth measurement using digital in-line holography and the hybrid method. Opt Express *21*, 26432-26449.

Gopalan, B., and Katz, J. (2010). Turbulent shearing of crude oil mixed with dispersants generates long microthreads and microdroplets. Phys Rev Lett. *104*.

Haigh, S.E., Salvi, S.S., Sevdali, M., Stark, M., Goulding, D., Clayton, J.D., Bullard, B., Sparrow, J.C., and Nongthomba, U. (2010). *Drosophila* indirect flight muscle specific *Act88F* actin mutants as a model system for studying congenital myopathies of the human *ACTA1* skeletal muscle actin gene. Neuromuscul Disord *20*, 363-374.

Katz, J., and Sheng, J. (2010). Applications of holography in fluid mechanics and particle dynamics. Annu Rev Fluid Mech *42*, 531-555.

Kron, S.J., and Spudich, J.A. (1986). Fluorescent actin-filaments move on myosin fixed to a glass-surface. Proc Natl Acad Sci USA *83*, 6272-6276.

Kumar, S.S., Sun, Y.N., Zou, S.G., and Hong, J.R. (2016). 3D holographic observatory for long-term monitoring of complex behaviors in *Drosophila*. Sci Rep-Uk *6*.

Liang, B., Chen, Y., Wang, C.K., Luo, Z., Regnier, M., Gordon, A.M., and Chase, P.B. (2003). Ca^{2+} regulation of rabbit skeletal muscle thin filament sliding: role of cross-bridge number. Biophys J 85, 1775-1786.

Malkiel, E., Sheng, I., Katz, J., and Strickler, J.R. (2003). The three-dimensional flow field generated by a feeding calanoid copepod measured using digital holography. J Exp Biol *206*, 3657-3666.

Meijering, E., Dzyubachyk, O., and Smal, I. (2012). Methods for cell and particle tracking. Method Enzymol *504*, 183-200.

Pardee, J.D., and Spudich, J.A. (1982). Purification of muscle actin. Method Cell Biol *24*, 271-289.

Razzaq, A., Schmitz, S., Veigel, C., Molloy, J.E., Geeves, M.A., and Sparrow, J.C. (1999). Actin residue glu(93) is identified as an amino acid affecting myosin binding. J Biol Chem *274*, 28321-28328.

Sheng, J., Malkiel, E., and Katz, J. (2006). Digital holographic microscope for measuring three-dimensional particle distributions and motions. Appl Optics *45*, 3893-3901.

Spudich, J.A., and Watt, S. (1971). The regulation of rabbit skeletal muscle contraction. I. Biochemical studies of the interaction of the tropomyosin-troponin complex with actin and the proteolytic fragments of myosin. J Biol Chem *246*, 4866-4871.

Viswanathan, M.C., Blice-Baum, A., Schmidt, W., Foster, B., and Cammarato, A. (2015). Pseudo-acetylation of K326 and K328 of actin disrupts *Drosophila melanogaster* indirect flight muscle structure and performance. Front Physiol *6*.

Vogel, S. (1966). Flight in *Drosophila* .1. Flight performance of tethered flies. J Exp Biol *44*, 567-&.

Vogler, G., and Ocorr, K. (2009). Visualizing the beating heart in *Drosophila*. J Vis Exp.